

Role of electron-phonon coupling in the thermal evolution of bulk Rashba-like spin-split lead halide perovskites exhibiting dual-band photoluminescence

Steele, Julian A.; Puech, Pascal; Monserrat, Bartomeu; Wu, Bo; Yang, Ruo Xi; Kirchartz, Thomas; Yuan, Haifeng; Fleury, Guillaume; Giovanni, David; Fron, Eduard; Keshavarz, Masoumeh; Debroye, Elke; Zhou, Guofu; Sum, Tze Chien; Walsh, Aron; Hofkens, Johan; Roeffaers, Maarten B. J.

2019

Steele, J. A., Puech, P., Monserrat, B., Wu., B., Yang, R. X., Kirchartz, T., . . . Roeffaers, M. B. J. (2019). Role of electron-phonon coupling in the thermal evolution of bulk Rashba-like spin-split lead halide perovskites exhibiting dual-band photoluminescence. *ACS Energy Letters*, 4(9), 2205-2212. doi:10.1021/acsenergylett.9b01427

<https://hdl.handle.net/10356/138055>

<https://doi.org/10.1021/acsenergylett.9b01427>

This document is the Accepted Manuscript version of a Published Work that appeared in final form in *ACS Energy Letters*, copyright © American Chemical Society after peer review and technical editing by the publisher. To access the final edited and published work see <https://doi.org/10.1021/acsenergylett.9b01427>

Downloaded on 09 Apr 2024 16:58:23 SGT

Role of Electron-Phonon Coupling in the Thermal Evolution of Bulk Rashba-Like Spin-Split Lead Halide Perovskites Exhibiting Dual-Band Photoluminescence

Julian A. Steele*,¹ Pascal Puech,² Bartomeu Monserrat,³ Bo Wu,⁴ Ruo Xi Yang,⁵ Thomas Kirchartz,^{6,7} Haifeng Yuan,⁸ Guillaume Fleury,¹ David Giovanni,⁹ Eduard Fron,⁸ Masoumeh Keshavarz,⁸ Elke Debroye,⁸ Guofu Zhou,⁴ Tze Chien Sum,⁹ Aron Walsh,^{10,11} Johan Hofkens,⁸ and Maarten B. J. Roeffaers*¹

Supporting Information

The Supporting Information is available free of charge on the ACS Publications website at DOI: XXXX

Experimental methods and additional figures and tables.

1) cMACS, Department of Microbial and Molecular Systems, KU Leuven, Celestijnenlaan 200F, 3001 Leuven, Belgium

2) CEMES/CNRS, Université de Toulouse, 29, rue Jeanne Marvig, 31055 Toulouse, France

3) TCM Group, Cavendish Laboratory, University of Cambridge, J. J. Thomson Avenue, Cambridge CB3 0HE, United Kingdom

4) Guangdong Provincial Key Laboratory of Optical Information Materials and Technology & Institute of Electronic Paper Displays, South China Academy of Advanced Optoelectronics, South China Normal University, Guangzhou 510006, P. R. China

5) Molecular Foundry, Lawrence Berkeley National Laboratory, 1 Cyclotron Road, Berkeley, CA, USA

6) IEK5-Photovoltaics, Forschungszentrum Jülich, 52425 Jülich, Germany

7) Faculty of Engineering and CENIDE, University of Duisburg-Essen, Carl-Benz-Straße 199, 47057 Duisburg, Germany

8) Department of Chemistry, KU Leuven, Celestijnenlaan 200F, Leuven, 3001, Belgium

9) Division of Physics and Applied Physics, School of Physical and Mathematical Sciences, Nanyang Technological University, 21 Nanyang Link, Singapore, 637371, Singapore

10) Department of Materials, Imperial College London, Exhibition Road, London SW7 2AZ, United Kingdom

11) Global E3 Institute and Department of Materials Science and Engineering, Yonsei University, Seoul 120-749, Korea

Email: julian.steele@kuleuven.be / maarten.roeffaers@kuleuven.be

ABSTRACT: The optoelectronic properties of lead halide perovskites strongly depend on their underlying crystal symmetries and dynamics, sometimes exhibiting a dual photoluminescence (PL) emission via Rashba-like effects. Here we exploit spin- and temperature-dependent PL to study single crystal APbBr₃ (A= Cs and methylammonium; CH₃NH₃) and evaluate peak energy, intensity and linewidth evolutions of their dual emission. Both perovskites exhibit temperature trends governed by two temperature regimes – above and below approximately 100 K – which impose different carrier scattering and radiative recombination dynamics. With increasing temperature, high-energy optical phonons activate near 100 K to drive energy splitting of the dual bands and induce linewidth broadening via electron-phonon coupling, with a stronger coupling constant inferred for carriers recombining by the spin-split indirect bands, compared to the direct ones. We find the unusual thermal evolutions of all-inorganic and hybrid bulk lead bromide perovskites are comparable – suggesting A-site independence and the dominance of dynamic effects – and are best understood within a framework which accounts for Rashba-like effects.

The interest for solution-processable lead halide perovskites within efficient solar cells^{1,2} stems from their promising optoelectronic response to sunlight and high tolerance to defects^{3,4}. This family of semiconductors are increasingly being considered as “soft” solid-state materials^{5–7}, whereby the fate of photo-generated charges primarily rely on the fundamental carrier-lattice interaction dynamics. For instance, polaron formation – via carrier-longitudinal-optical-phonon (Fröhlich) interactions – within the lattice has been linked to several favourable qualities, like long carrier lifetimes and diffusion lengths^{8–10}. Recent indications of spin splitting and indirect tail state formation in lead halide perovskites^{11–16} due to Rashba-like effects¹⁷ motivate a reconsideration of how electron-phonon coupling can exist within its perturbed electronic band structure. Universally, for the application of any polar metal halide perovskite, the properties of the free charge carriers and phonon scattering mechanisms are central to its optoelectronic performance at room temperature (RT).

Bulk Rashba-like effects occur in metal halide perovskites via two key ingredients. First, heavy elements, like Pb, introduce strong spin–orbit coupling (SOC) into the electronic structure. Second, the crystal must lack inversion symmetry, so that an effective magnetic field is imposed on electrons by SOC, lifting spin degeneracy and splitting the band electronic structure (Figure 1). To lose inversion symmetry, both static¹⁸ (i.e. intrinsically non-centrosymmetric) and dynamic^{12,13,19} (i.e. fluctuating local breaks in symmetry) mechanisms have been proposed, though the full picture is still debated²⁰. Consequently, the valence band maxima²¹ (VBM) and conduction band minima (CBM) shift away from the high-symmetry points in the Brillouin zone, giving rise to low-energy indirect tail states^{11,15} (Figure 1). The shift for Pb-based perovskites in reciprocal space is expected to be larger for the CBM compared to the VBM due to the relative orbital contributions to the band structure²², producing a low energy (LE) indirect transition alongside a high energy (HE) direct one. Notably, these phenomena constitute a general result within both all-inorganic and hybrid lead halide perovskites, leading to a characteristic dual photoluminescence (PL) emission^{11,15} which is better seen at low temperatures²³.

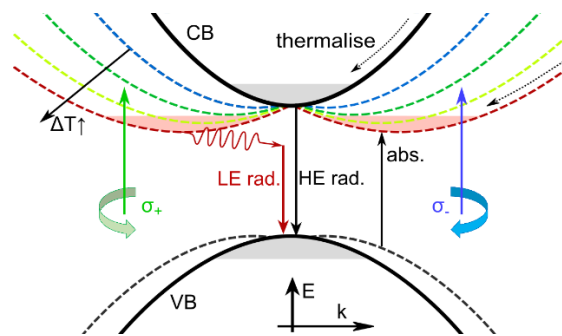


Figure 1: Schematic of energy band structure experiencing thermally-driven Rashba-like spin splitting, with selective excitation provided using left (σ_+) and right (σ_-) circularly polarised light. Photo-generated carriers recombine by two main radiative (rad.) pathways; a high-energy (HE) unperturbed direct bandgap transition, and a phonon-mediated low-energy (LE) indirect bandgap. For simplicity, only the CB splitting shows a thermal dependence.

The origin of the spin splitting in bulk hybrid lead halide perovskites like MAPbBr₃ (where MA is methylammonium; CH₃NH₃) is unclear, and is especially puzzling for all-

inorganic CsPbBr₃, which adopts a centrosymmetric orthorhombic (*Pnma*) crystal structure²⁴ at RT. However, it is expected that the thermal motion of the Cs⁺ atoms (as well as MA molecules) at the cation A-sites couple to lattice vibrations to promote local polar fluctuations²⁵ (Figure 2a inset) and dynamically break local centrosymmetry^{13,16}. It is not known if CsPbBr₃ or MAPbBr₃ adopt a “static” centrosymmetric structure near 0 K¹¹. The intensity of the Rashba-induced LE peak is sensitive to sample preparation¹¹, being best resolved in large single crystals (SCs)²⁶. As such, PL-based studies^{27,28} become ambiguous when comparing across different physical microstructures, i.e. nanocrystals or polycrystalline networks. Nevertheless, accounting for Rashba-like effects that underpin the low-temperature dual PL emission in CsPbBr₃ and MAPbBr₃ will yield a more accurate description of the photophysics involved^{29,30}.

In this Letter, we report a spin- and temperature-dependent PL analysis of the emission positions, linewidths and intensities arising in SC all-inorganic CsPbBr₃ and hybrid MAPbBr₃ perovskites possessing dual bands at RT. The two systems exhibit a comparable dependence on temperature, inferring that the underlying models employed are cation-independent and strongly driven by lattice dynamics. The LE and HE peak positions undergo different evolutions in the lead bromide perovskites, whereby both peaks blueshift when warming above 0 K, with LE undertaking an additional strong redshift above 100 K, with the activation of high-energy optical phonons. While high-temperature quenching of the LE emission intensity is in-line with typical semiconducting behaviour, we assign thermal-driven intersystem crossing to account for a HE intensity which peaks near 100 K and quenches when approaching 0 K. The Fröhlich coupling strength of carriers residing in the spin-split bands is found to be much higher than in the direct bands in CsPbBr₃, inferred from the temperature-dependent linewidth broadening. We demonstrate that several anomalous features in the low-temperature dual PL emission evolution found in SC CsPbBr₃ and MAPbBr₃ are best understood when Rashba-like effects are considered.

APbBr₃ (A = Cs and MA) SCs were prepared with a modified recipe from literature³¹, resulting in 1-3 mm-sized perovskite single crystals (Methods and Figure S1 of Supporting Information).

Figure 2(a) provides the RT PL spectrum of CsPbBr₃, displaying a clear dual emission.¹¹ At RT, the emission full width at half maximum (FWHM: Γ) will be dominated³² by the Fröhlich interaction strength, represented by dimensionless constant α , which scales with the carrier effective mass (m^*) according to the Feynman polaron model³³ as

$$\alpha = \frac{e^2}{\hbar c} \sqrt{\frac{m^* c}{2\hbar\omega_{LO}}} \left(\frac{1}{\varepsilon_\infty} - \frac{1}{\varepsilon_0} \right). \quad (1)$$

Parameters ε_∞ and ε_0 respectively indicate the high-frequency and static dielectric constants, c the speed of light, \hbar the reduced Planck constant, e the fundamental charge, and ω_{LO} is the frequency of the coupling optical phonon mode(s) involved. The decisive factor for m^* is the E - k dispersion curvature at the CB and VB extrema (assuming near-parabolic character), whereby: $m^*(k) \propto (\partial^2 E / \partial k^2)^{-1}$.

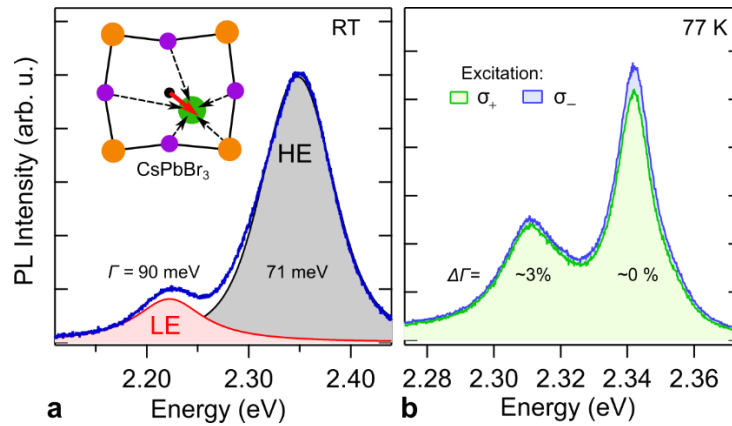


Figure 2: (a) Room-temperature PL spectrum of SC CsPbBr₃ ($\lambda_{\text{exc.}} = 400$ nm) with dual high- (HE) and low-energy (LE) emissions, with their FWHM (Γ) indicated. The inset illustrates how the perovskite “cage” (Pb-Br framework) and dynamic symmetry breaking¹³ of an off-centre Cs cation (green) creates an effective electric dipole moment (solid red arrow), through the summation of local dipoles (dashed arrows). (b) Right circularly polarised PL spectra (77 K) of CsPbBr₃ upon exciting (473 nm) with left (σ^+) and right (σ^-) circularly polarised light. The $\Delta\Gamma$ values depict the difference in the linewidth derived from their fitting: $\Delta\Gamma = 2[\Gamma(\sigma^-) - \Gamma(\sigma^+)]/[\Gamma(\sigma^-) + \Gamma(\sigma^+)]$.

Within the spin-split system depicted in Figure 1, a one-band effective mass approximation no longer holds³⁴ for Equation 1, given two shallow side valleys are formed. For example, carriers thermalizing into each Rashba-induced valley will have nontrivial spin texture, with intervalley scattering mediated via phonons. Importantly, for the spin-split bands, their curvature is expected to be small compared to the direct transition^{19,35}, indicating an increase in the effective mass and a relative increase of the Fröhlich interaction. In Figure 2(a), the linewidth of LE is relatively larger than that of HE at RT.

The effective mass of charges in the two spin-split indirect bands will evolve as a function of the SOC, described by the Rashba Hamiltonian³⁴. Both the electron-phonon coupling^{36,37} and the (large) polaronic effective mass³⁸ correction are enhanced by Rashba-like effects. In this scenario, the relative electron-phonon coupling strength for carrier in the lower (-) Rashba band are expected to be larger than those in the upper (+) one³⁸. As a results, carriers recombining at the two spin-split band edges will encounter different polaron effects, leading to stronger coupling and a broader PL emission arising from recombination via the lower branch. We experimentally assess this via a comparison of the LE emission full-width at half maximum (FWHM; Γ) when the recombination has different spin populations, down at cryogenic temperatures ($T = 77$ K) where the LE band is more pronounced. To exclude instrumental response to light helicity, we fixed the detection optics and only vary the incident polarisation. Figure 2(b) displays right circularly polarised PL spectra recorded from CsPbBr₃ using left (σ_+) and right (σ_-) circularly-polarised excitation. Beyond the polarisation-dependence of the emission intensities¹¹, fitting these data (Voigt functions) reveals an approximately 3 % broader LE peak using σ_- excitation compared to σ_+ , with no detectable change in the HE linewidth. While this difference is relatively small (the indirect recombination rate will occur relatively slowly compared to the rate of spin-flipping), it is consistent with a relative disparity in the electron-phonon coupling arising from the two spin valleys, and should be enhanced exciting closer to the split band edges¹¹.

Smearing the spin information, Figure 3(a) overviews the unpolarised temperature-dependence of the normalised PL lineshape recorded from SC CsPbBr₃ and MAPbBr₃ (raw spectra shown in Figure S2). A low-energy shoulder on the MAPbBr₃ HE peak appears and grows at relatively low temperatures, a feature which is location dependent on the crystal surface (Figure S3). Fitting the HE band of MAPbBr₃ with an additional peak reveals this feature to closely track the thermally-driven energy shift of HE (Figure 3(b)) and is respectively redshifted by ~15 meV (at lower temperatures where it is better resolved). The paralleled evolution and the relative energy shift (i.e. close to the characteristic optical phonon energies³⁹) of this peak is consistent with the formation of a low-energy satellite band, attributable to phonon replicas^{40,41} (identified as HE'). While similar behavior is not exhibited in the SC CsPbBr₃ PL emission, their overall thermal evolutions are fairly comparable⁴² and are thus evaluated together.

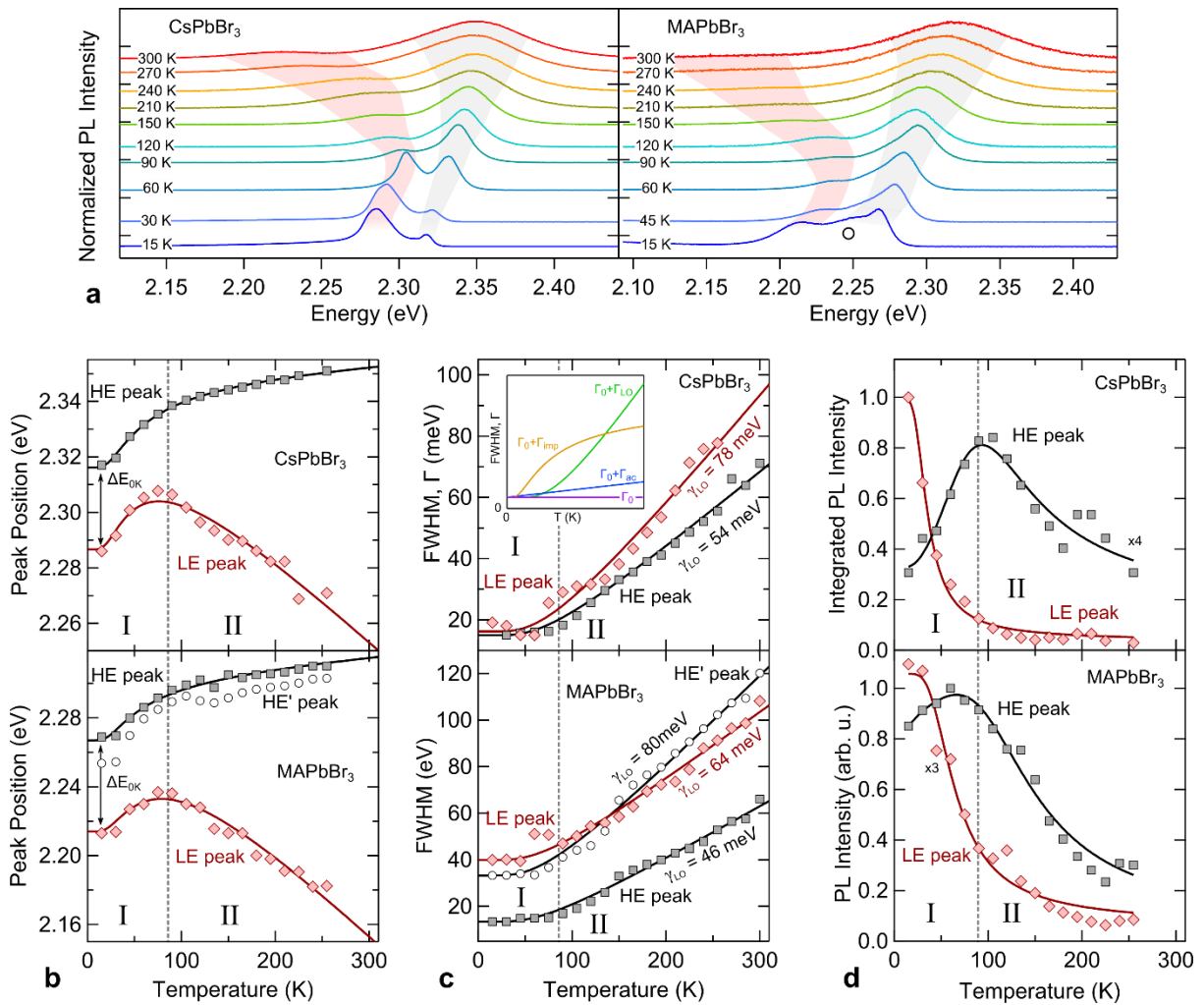


Figure 3: (a) Normalised low-temperature PL spectra of single crystal CsPbBr₃ and MAPbBr₃ ($\lambda_{\text{exc.}} = 400 \text{ nm} / 3.1 \text{ eV}$), with the open circle in the MAPbBr₃ data set highlighting the phonon replica peak (HE') at low-temperatures. Analysis of the temperature evolution for both material systems; (b) Emission peak energies modelled using Equation 3, including the feature identified in (a) by the open circle; (c) FWHM of the dual bands fit via Equation 5; (d) Normalised integrated LE and HE peak intensities, fit using Equations 6 and 7, respectively. For MAPbBr₃, the integration of HE includes the signal of its satellite peak. For each analysis, low-temperature and high-temperature trends are respectively identified by regimes I and II. The inset in (c) shows the archetypal form of the temperature dependence of each contributing term in Equation 5.

The LE and HE peak positions undergo different evolutions in Figure 3(b), due to the superposition of two identified trends. Trend I raises the energy of both peaks, due to a blueshift in the absorption edge with increasing temperature, driven by a combination of thermal expansion and electron-phonon coupling^{37,43,44}. LE experiences an additional redshift in regime II at higher temperatures, representing a thermally-induced band splitting¹¹ superimposed to the aforementioned blueshift. Both effects are activated by phonons with “effective” vibrational energies ($\hbar\omega$) – via electron-phonon coupling – although the respective mode(s) involved are very different. For instance, any phonon mode (acoustic or optical) can raise the lead halide perovskite bandgap energy with increasing temperature^{27,37}; however, high-temperature Rashba-like effects must involve modes that break local inversion symmetry¹⁹.

The respective phonon population is governed by Bose–Einstein statistics:

$$n(T) = \frac{1}{e^{\hbar\omega/k_B T} - 1}, \quad (2)$$

where k_B is the Boltzmann constant. Warming above absolute zero, low-energy acoustic phonons dominate the initial rise in bandgap energy^{27,37,45}. At higher temperatures, optical phonons and spin splitting become more influential, inverting the relative shift in LE¹¹. This infers that trend I needs only relatively low phonon energies, while trend II requires relatively high-frequency modes.

Considering the interaction of electrons with the crystal lattice, the temperature dependence of the emission peaks can be reduced to the Bose-Einstein bandgap model^{46,47}:

$$E(T) = E_0 + \sum_i A_i \left(\frac{1}{e^{\hbar\omega_i/k_B T} - 1} + \frac{1}{2} \right). \quad (3)$$

For up to 3 Bose-Einstein oscillators ω_i ($i = 1, 2, 3$), A_i represents their weight which, if negative (positive), describes the degree of the energy decrease (increase) with rising temperature, and E_0 is the bandgap energy at 0 K. The evolution of HE will involve the summation of a low-energy acoustic phonon branch ($i = 1$) and a higher energy optical phonon one ($i = 2$), with opposite weightings. LE initially follows the shift of HE, though is redshifted by a third relatively high-energy oscillator ($i = 3$) during trend II. Therefore, the two Bose-Einstein terms used to account for HE are used as inputs to evaluate their combined influence on LE (fitting parameters in Table S1). The effective phonon frequencies shifting HE (CsPbBr₃; $\hbar\omega_1 = 3.8$ meV, $\hbar\omega_2 = 7.0$ meV, and MAPbBr₃; $\hbar\omega_1 = 3.6$ meV, $\hbar\omega_2 = 6.4$ meV) are estimated to be far smaller than the phonons driving the LE redshift (CsPbBr₃; $\hbar\omega_3 = 14.7$ meV, and MAPbBr₃; $\hbar\omega_3 = 11.3$ meV). We note the potential involvement of high-energy Raman active optical modes nearing this energy (Figure S4 and S5), whose population will be relatively small below 100 K, in line with the two different regimes identified in the model. Interestingly, the HE and LE peaks in Figure 3(b) approach an intrinsic energy-split near zero temperature¹¹; $\Delta E_{0K} = 30$ meV for CsPbBr₃, while $\Delta E_{0K} = 55$ meV for MAPbBr₃. While dynamic effects arising from thermal fluctuations are suppressed with decreasing temperature, this does not mean that all dynamic effects vanish in quantum systems. Even at absolute zero there are dynamic fluctuations arising from quantum zero-point motion. This comes from predictions made for the perovskites under consideration¹⁹ and are based on the intrinsic dynamic disorder and peak energy splitting at 0 K. More generally, quantum zero-point fluctuations are known to play a major role in other perovskite materials, with the best known example being SrTiO₃, which is a quantum paraelectric in which quantum fluctuations stabilise the paraelectric phase compared to the ferroelectric phase⁴⁸. Alternatively, in the absence of clear structural data for these materials near 0 K, the energy split may potentially come about

by a loss of centrosymmetry in the local crystal structure. However, because the dual peak evolution is common to both all-inorganic CsPbBr₃ and hybrid MAPbBr₃ materials, this result reinforces the interpretation of “dynamical” spin splitting in the Cs case, as MA statically breaks inversion symmetry due to the dipole in the MA molecule, whereas Cs does not statically break inversion symmetry (i.e. spherical atom). The paralleled behaviour of both systems shows that with the inclusion of dynamics, the physics becomes the same, and is in all cases dominated by the dynamical spin splitting.

Assessing the temperature-dependent emission broadening in Figure 3(c), the intrinsic FWHM (Γ_0) of both perovskites grow with increasing temperatures. In Figure 3(c), the LE emission from both CsPbBr₃ and MAPbBr₃ broadens faster than HE with rising temperature, suggesting enhanced carrier scattering in these bands. The temperature-dependent excitonic linewidth of band-to-band transitions within semiconductors^{32,49} is relatively well understood, being described by

$$\begin{aligned}\Gamma(T) &= \Gamma_0 + \Gamma_{ac} + \Gamma_{LO} + \Gamma_{imp} \\ &= \Gamma_0 + \gamma_{ac}T + \gamma_{LO}n(T) + \gamma_{imp}e^{-E_b/k_B T}.\end{aligned}\quad (4)$$

The second and third terms (Γ_{ac} and Γ_{LO}) respectively describe the trends ascribed to acoustic and LO-phonon (Fröhlich) scattering, with coupling strengths γ_{ac} and γ_{LO} . The fourth term accounts for the scattering from ionized impurities, with average binding energy E_b . Below 75 K, the linear Γ_{ac} component – involving low-energy acoustic phonons – will dominate the broadening. The gradient of the of the FWHM of all peaks is relatively flat in regime I, in-line with negligible contributions from the γ_{ac} term^{32,50–52} and is omitted for simplicity. The small sublinear feature in LE below 100 K for both CsPbBr₃ and MAPbBr₃ resembles the influence of Γ_{imp} (inset of Figure 3(d)), but does not appear in HE. Because it is unlikely that ionised impurities will selectively scatter carriers residing only in the LE bands, this feature is suggested to have other origins and we omit for simplicity³². There is a group of distinct LO-optical vibrations expected to interact with charge carriers⁵³ (Figure S4 and S5) in lead

bromide perovskites with energies close to 17 meV ($\sim 140 \text{ cm}^{-1}$). As well, the energy of the optical phonon band is stable down to cryogenic temperatures. Therefore, we adopt a simplified model to fit our data³², dependent on two dominant components:

$$\Gamma(T) = \Gamma_0 + \frac{\gamma_{LO}}{e^{\hbar\omega_{LO}/k_B T} - 1}. \quad (5)$$

For the LE band, a temperature invariant γ_{LO} broadening parameter may not fully describe its behaviour over the temperature range explored, as its nature depends on the phonon population. However, the broadening of LE above 100 K is fairly linear in both CsPbBr₃ and MAPbBr₃, being agreeably fit by a fixed γ_{LO} parameter. We note that analogous models have been used for heavy- and light-hole VB splitting in strained epitaxial semiconductors and quantum wells⁵⁴, which experience temperature-dependent changes in their band dispersion at the high-symmetry points.

Through Equation 5 we estimate the relative strength of the Fröhlich coupling arising in the two recombination pathways in CsPbBr₃; γ_{LO} is revealed to be $54 \pm 5 \text{ meV}$ for the direct HE transition and $78 \pm 8 \text{ meV}$ from the LE linewidth broadening. Likewise, for MAPbBr₃; γ_{LO} is determined to be $46 \pm 3 \text{ meV}$ and $59 \pm 6 \text{ meV}$ for HE and LE, respectively, and relatively larger at $80 \pm 10 \text{ meV}$ for the HE' satellite. The large difference in coupling strength between the direct HE and spin-split LE emissions from both these perovskites is expected within a phonon-driven broadening model which corrects for SOC, i.e. making the Rashba band broaden faster, via stronger Fröhlich coupling. However, the sensitivity of the LE emission to the sample preparation¹¹ may explain the large spread in γ_{LO} values reported^{32,51,52,55–58} from low-temperature PL analysis of these materials, reported reaching as high as 130 meV ⁵⁹.

Figure 3(a) shows that the relative weighting of the normalized LE band significantly grows for both SC CsPbBr₃ and MAPbBr₃ perovskites upon cooling, which is tracked in Figure 3(d) (note the MAPbBr₃ HE intensity is derived from the combined integrated emission of both HE and HE' bands). First considering the more standard characteristic of the LE bands, the initial

intensity (I_0) decreases above 0 K due to thermally activated quenching (estimated via a single dominant non-radiative channel), commonly described by an Arrhenius expression:

$$I(T) = \frac{I_0}{1 + ae^{-E_a/k_B T}}, \quad (6)$$

where a is the ratio of non-radiative and radiative probabilities and E_a is the activation energy of the quenching channel. Applying Equation 6 to the temperature dependence of the LE intensity yields an activation energy of 11 meV for CsPbBr₃ and 18 meV for MAPbBr₃ (Table S2).

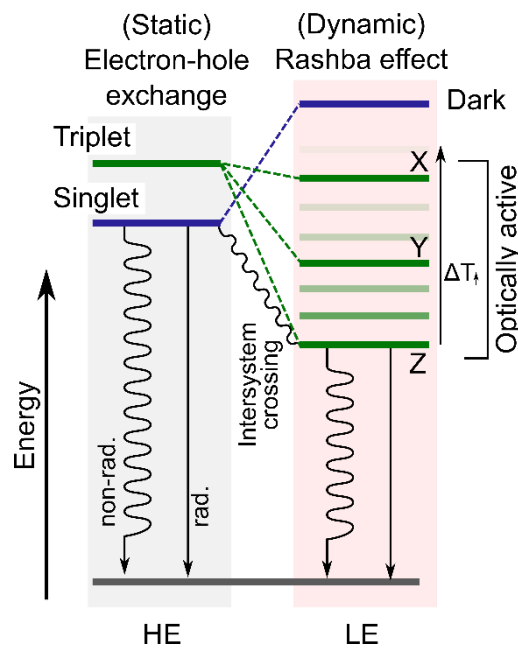


Figure 4: The expected fine structure⁶⁰ of the band-edge excitons considering short- and long-range electron-hole exchange (left) and then including Rashba-like effects⁶¹ with dynamic symmetry breaking along the z direction (right), under orthorhombic symmetry. In the split states (dynamic), the exciton separates into three bright states and a high-energy dark state. Intersystem crossing will depend on the relative population of the low-energy spin split triplet states, which is governed by the crystal temperature.

The temperature dependence of the HE emissions, on the other hand, is more complex; the HE peak intensity maximises under 100 K and begins to quench moving to either lower (regime I) and higher (regime II) temperatures. At higher temperatures, the HE intensity decrease is similar to LE, manifesting via indiscriminate thermally activated non-radiative carrier

recombination. In regime I, however, the system is subject to another non-radiative channel which becomes more significant upon approaching 0 K. The Arrhenius fitting can be modified to include the second quenching term, whereby

$$I(T) = \frac{I_0}{1 + a_1 e^{-\frac{E_{a1}}{k_B T}} + a_2 e^{-\frac{E_{a2}}{k_B T}}} . \quad (7)$$

The two competing processes ($a_1 > 0$; $a_2 < 0$) superimpose to yield a maximum below 100 K, with the fitting parameters provided in Table S2.

The origin of the non-radiative channel quenching in regime I for both CsPbBr₃ and MAPbBr₃ is difficult to isolate, though it is likely connected to thermally-driven intersystem crossing between the bright low-energy spin-split triplet states and the bright direct transition involving a singlet state⁶⁰. This is because the intersystem crossing between the states is mediated by optical phonons, which are depopulated and disappear toward 0 K. Based on the predicted exciton fine structure of CsPbBr₃ perovskite^{60–63}, an energy scheme representing this proposition is displayed in Figure 4. The left and right portions of the scheme represent the static and dynamic cases of the electronic structure, which generate the unperturbed and perturbed band structures in Figure 1, respectively. As shown in Figure 4, thermal energy is required to populate the low-energy Rashba bands and allow intersystem crossing to the static HE states, thus facilitating a more intense HE emission. This is because the band structure remains split at 0 K, retaining the lower energy indirect tail states shown in Figure 1. That is to say, some of the rise in the low-energy emission intensity while cooling in regime I is at the cost of depopulating the radiative high-energy transition.

In summary, we have reported a low-temperature PL analysis of high-quality single crystals of CsPbBr₃ and MAPbBr₃ emitting a dual emission accounting for Rashba-like effects. The thermal evolution of the two perovskites – one being an all-inorganic system and the other a hybrid – are very comparable, suggesting that the underlying physics of the temperature dependence is cation-independent and dominated by dynamics, in line with recent predictions. We find that a single-band-to-band model no longer accounts for the radiative recombination

pathways expressed in APbBr₃ perovskites, due to different physical properties of carriers residing in the split band structure. While the formation of indirect tail states promotes longer radiative lifetimes¹⁴, it ultimately enhances electron-phonon scattering, reducing carrier mobility and leads to a relatively broad low-energy emission. To explain the origin of this behaviour, we connect both the enhancement in the effective mass of carriers residing in the spin-split bands and the requirement for additional scattering to overlap the bands, for recombination. Further, the direct band-edge recombination is quenched near 0 K, which we attribute to the presence of an unpopulated low-energy indirect emission pathway. These findings allow rationalization of previous experimental observations and provide a key to understanding the complex carrier dynamics in bulk spin-split halide perovskites.

1. Green, M. A., Ho-Baillie, A. & Snaith, H. J. The emergence of perovskite solar cells. *Nat Photon* **8**, 506–514 (2014).
2. Meredith, P. & Armin, A. Scaling of next generation solution processed organic and perovskite solar cells. *Nature Communications* **9**, 5261 (2018).
3. Kang, J. & Wang, L.-W. High Defect Tolerance in Lead Halide Perovskite CsPbBr₃. *The Journal of Physical Chemistry Letters* **8**, 489–493 (2017).
4. Walsh, A. & Zunger, A. Instilling defect tolerance in new compounds. *Nature Materials* **16**, 964–967 (2017).
5. Miyata, K., Atallah, T. L. & Zhu, X. Y. Lead halide perovskites: Crystal-liquid duality, phonon glass electron crystals, and large polaron formation. *Science Advances* **3**, e1701469 (2017).
6. Miyata, K. *et al.* Large polarons in lead halide perovskites. *Science Advances* **3**, e1701217 (2017).
7. Frost, J. M. & Walsh, A. What Is Moving in Hybrid Halide Perovskite Solar Cells? *Accounts of Chemical Research* **49**, 528–535 (2016).

8. Zhu, H. *et al.* Screening in crystalline liquids protects energetic carriers in hybrid perovskites. *Science* **353**, 1409–1413 (2016).
9. Zhu, X.-Y. & Podzorov, V. Charge Carriers in Hybrid Organic–Inorganic Lead Halide Perovskites Might Be Protected as Large Polarons. *J. Phys. Chem. Lett.* **6**, 4758–4761 (2015).
10. Stranks, S. D. *et al.* Electron-Hole Diffusion Lengths Exceeding 1 Micrometer in an Organometal Trihalide Perovskite Absorber. *Science* **342**, 341–344 (2013).
11. Wu, B. *et al.* Indirect tail states formation by thermal-induced polar fluctuations in halide perovskites. *Nature Communications* **10**, 484 (2019).
12. Niesner, D. *et al.* Structural fluctuations cause spin-split states in tetragonal $(\text{CH}_3\text{NH}_3)_2\text{PbI}_3$ as evidenced by the circular photogalvanic effect. *Proceedings of the National Academy of Sciences* **115**, 9509–9514 (2018).
13. McKechnie, S. *et al.* Dynamic symmetry breaking and spin splitting in metal halide perovskites. *Physical Review B* **98**, 085108 (2018).
14. Zheng, F., Tan, L. Z., Liu, S. & Rappe, A. M. Rashba Spin–Orbit Coupling Enhanced Carrier Lifetime in $\text{CH}_3\text{NH}_3\text{PbI}_3$. *Nano Letters* **15**, 7794–7800 (2015).
15. Wang, T. *et al.* Indirect to direct bandgap transition in methylammonium lead halide perovskite. *Energy & Environmental Science* **10**, 509–515 (2017).
16. Isarov, M. *et al.* Rashba Effect in a Single Colloidal CsPbBr_3 Perovskite Nanocrystal Detected by Magneto-Optical Measurements. *Nano Lett.* **17**, 5020–5026 (2017).
17. Niesner, D. *et al.* Giant Rashba Splitting in $\text{CH}_3\text{NH}_3\text{PbBr}_3$ Organic-Inorganic Perovskite. *Phys. Rev. Lett.* **117**, 126401 (2016).
18. Röhm, H. *et al.* Ferroelectric Properties of Perovskite Thin Films and Their Implications for Solar Energy Conversion. *Advanced Materials* 1806661 (2019).
doi:10.1002/adma.201806661

19. Monserrat, B. & Vanderbilt, D. Phonon-assisted spin splitting in centrosymmetric crystals. *arXiv:1711.06274 [cond-mat]* (2017).
20. Frohna, K. *et al.* Inversion symmetry and bulk Rashba effect in methylammonium lead iodide perovskite single crystals. *Nature Communications* **9**, 1829 (2018).
21. Zhang, X., Shen, J.-X., Wang, W. & Van de Walle, C. G. First-Principles Analysis of Radiative Recombination in Lead-Halide Perovskites. *ACS Energy Letters* **3**, 2329–2334 (2018).
22. Azarhoosh, P., McKechnie, S., Frost, J. M., Walsh, A. & van Schilfgaarde, M. Research Update: Relativistic origin of slow electron-hole recombination in hybrid halide perovskite solar cells. *APL Materials* **4**, 091501 (2016).
23. Dar, M. I. *et al.* Origin of unusual bandgap shift and dual emission in organic-inorganic lead halide perovskites. *Science Advances* **2**, e1601156 (2016).
24. Stoumpos, C. C. *et al.* Crystal Growth of the Perovskite Semiconductor CsPbBr₃: A New Material for High-Energy Radiation Detection. *Crystal Growth & Design* **13**, 2722–2727 (2013).
25. Yaffe, O. *et al.* Local Polar Fluctuations in Lead Halide Perovskite Crystals. *Physical Review Letters* **118**, 136001 (2017).
26. Thu Ha Do, T. *et al.* Optical study on intrinsic exciton states in high-quality CH₃NH₃PbBr₃ single crystals. *Physical Review B* **96**, 075308 (2017).
27. Diroll, B. T., Zhou, H. & Schaller, R. D. Low-Temperature Absorption, Photoluminescence, and Lifetime of CsPbX₃ (X = Cl, Br, I) Nanocrystals. *Advanced Functional Materials* **28**, 1800945 (2018).
28. Sebastian, M. *et al.* Excitonic emissions and above-band-gap luminescence in the single-crystal perovskite semiconductors CsPbBr₃ and CsPbCl₃. *Physical Review B - Condensed Matter and Materials Physics* **92**, 235210 (2015).

29. Yu, Z.-G. Rashba Effect and Carrier Mobility in Hybrid Organic–Inorganic Perovskites. *J. Phys. Chem. Lett.* **7**, 3078–3083 (2016).
30. Yu, Z.-G. The Rashba effect and indirect electron–hole recombination in hybrid organic–inorganic perovskites. *Phys. Chem. Chem. Phys.* **19**, 14907–14912 (2017).
31. Rakita, Y. *et al.* Low-Temperature Solution-Grown CsPbBr₃ Single Crystals and Their Characterization. *Crystal Growth and Design* **16**, 5717–5725 (2016).
32. Wright, A. D. *et al.* Electron-phonon coupling in hybrid lead halide perovskites. *Nature Communications* **7**, 11755 (2016).
33. Feynman, R. P. Slow Electrons in a Polar Crystal. *Physical Review* **97**, 660–665 (1955).
34. Yu A Bychkov & ÉI Rashba. Properties of a 2D electron gas with lifted spectral degeneracy. *JETP lett* **39**, 78 (1984).
35. Monserrat, B. & Vanderbilt, D. Temperature dependence of the bulk Rashba splitting in the bismuth tellurohalides. *Physical Review Materials* **1**, 054201 (2017).
36. Covaci, L. & Berciu, M. Polaron Formation in the Presence of Rashba Spin-Orbit Coupling: Implications for Spintronics. *Physical Review Letters* **102**, 186403 (2009).
37. Saidi, W. A., Poncé, S. & Monserrat, B. Temperature Dependence of the Energy Levels of Methylammonium Lead Iodide Perovskite from First-Principles. *The Journal of Physical Chemistry Letters* **7**, 5247–5252 (2016).
38. Li, Z., Ma, Z., Wright, A. R. & Zhang, C. Spin-orbit interaction enhanced polaron effect in two-dimensional semiconductors. *Applied Physics Letters* **90**, 112103 (2007).
39. Brivio, F. *et al.* Lattice dynamics and vibrational spectra of the orthorhombic, tetragonal, and cubic phases of methylammonium lead iodide. *Physical Review B* **92**, 144308 (2015).
40. Lozhkina, O. A. *et al.* Low Inhomogeneous Broadening of Excitonic Resonance in MAPbBr₃ Single Crystals. *J. Phys. Chem. Lett.* **9**, 302–305 (2018).

41. Iaru, C. M., Geuchies, J. J., Koenraad, P. M., Vanmaekelbergh, D. & Silov, A. Y. Strong Carrier-Phonon Coupling in Lead Halide Perovskite Nanocrystals. *ACS Nano* **11**, 11024–11030 (2017).
42. Guo, Y. *et al.* Dynamic emission Stokes shift and liquid-like dielectric solvation of band edge carriers in lead-halide perovskites. *Nature Communications* **10**, 1175 (2019).
43. Milot, R. L., Eperon, G. E., Snaith, H. J., Johnston, M. B. & Herz, L. M. Temperature-Dependent Charge-Carrier Dynamics in CH₃NH₃PbI₃ Perovskite Thin Films. *Advanced Functional Materials* **25**, 6218–6227 (2015).
44. Foley, B. J. *et al.* Temperature dependent energy levels of methylammonium lead iodide perovskite. *Applied Physics Letters* **106**, 243904 (2015).
45. Saidi, W. A. & Kachmar, A. Effects of Electron–Phonon Coupling on Electronic Properties of Methylammonium Lead Iodide Perovskites. *The Journal of Physical Chemistry Letters* **9**, 7090–7097 (2018).
46. Lautenschlager, P., Garriga, M., Logothetidis, S. & Cardona, M. Interband critical points of GaAs and their temperature dependence. *Physical Review B* **35**, 9174–9189 (1987).
47. Bhosale, J. *et al.* Temperature dependence of band gaps in semiconductors: Electron-phonon interaction. *Physical Review B* **86**, 195208 (2012).
48. Müller, K. A. & Burkard, H. SrTiO₃ : An intrinsic quantum paraelectric below 4 K. *Phys. Rev. B* **19**, 3593–3602 (1979).
49. Rudin, S. & Reinecke, T. L. Temperature-dependent exciton linewidths in semiconductor quantum wells. *Physical Review B* **41**, 3017–3027 (1990).
50. Han, Q., Wu, W., Liu, W., Yang, Q. & Yang, Y. Temperature-dependent photoluminescence of CsPbX₃ nanocrystal films. *Journal of Luminescence* **198**, 350–356 (2018).

51. Ramade, J. *et al.* Exciton-phonon coupling in a CsPbBr₃ single nanocrystal. *Applied Physics Letters* **112**, 072104 (2018).
52. Wolf, C. & Lee, T.-W. Exciton and lattice dynamics in low-temperature processable CsPbBr₃ thin-films. *Materials Today Energy* **7**, 199–207 (2018).
53. Schlipf, M., Poncé, S. & Giustino, F. Carrier Lifetimes and Polaronic Mass Enhancement in the Hybrid Halide Perovskite CH₃NH₃PbI₃ from Multiphonon Fröhlich Coupling. *Physical Review Letters* **121**, 086402 (2018).
54. Lee, J., Koteles, E. S. & Vassell, M. O. Luminescence linewidths of excitons in GaAs quantum wells below 150 K. *Physical Review B* **33**, 5512–5516 (1986).
55. Ghosh, S. *et al.* Phonon Coupling with Excitons and Free Carriers in Formamidinium Lead Bromide Perovskite Nanocrystals. *J. Phys. Chem. Lett.* **9**, 4245–4250 (2018).
56. Zhang, F. *et al.* Silica coating enhances the stability of inorganic perovskite nanocrystals for efficient and stable down-conversion in white light-emitting devices. *Nanoscale* **10**, 20131–20139 (2018).
57. Qiuju Han, Wu, W., Weilong Liu & Qingxin Yang. Temperature-dependent photoluminescence of CsPbX₃ nanocrystal films. *Journal of Luminescence* **198**, 350–356 (2018).
58. Lee, S. M. *et al.* Temperature-Dependent Photoluminescence of Cesium Lead Halide Perovskite Quantum Dots: Splitting of the Photoluminescence Peaks of CsPbBr₃ and CsPb(Br/I)₃ Quantum Dots at Low Temperature. *J. Phys. Chem. C* **121**, 26054–26062 (2017).
59. Wei, K. *et al.* Temperature-dependent excitonic photoluminescence excited by two-photon absorption in perovskite CsPbBr₃ quantum dots. *Opt. Lett.* **41**, 3821 (2016).
60. Becker, M. A. *et al.* Bright triplet excitons in caesium lead halide perovskites. *Nature* **553**, 189–193 (2018).

61. Sercel, P. C. *et al.* Exciton Fine Structure in Perovskite Nanocrystals. *Nano Lett.* **19**, 4068–4077 (2019).
62. Utzat, H. *et al.* Coherent single-photon emission from colloidal lead halide perovskite quantum dots. *Science* **363**, 1068–1072 (2019).
63. Tamarat, P. *et al.* The ground exciton state of formamidinium lead bromide perovskite nanocrystals is a singlet dark state. *Nature Materials* **18**, 717–724 (2019).

Acknowledgements The authors acknowledge financial support from the Research Foundation-Flanders (FWO, Grant Nos. 12Y7218N, G.0B39.15, G.0197.11 and 12O3719N postdoctoral fellowship to J.A.S., C.M., H.Y. and E.D.), KU Leuven Research Fund (C14/15/053), the Flemish government through long term structural funding Methusalem (CASAS2, Meth/15/04), the Hercules foundation (HER/11/14), and the Belgian Federal Science Policy Office (IAP-VII/05). The research leading to these results has received funding from the European Research Council under the European Union's Seventh Framework Programme (FP/2007-2013)/ERC Grant Agreement (Grant No. 307523). B.M. acknowledges support from the Winton Programme for the Physics of Sustainability and from Robinson College, Cambridge, and the Cambridge Philosophical Society for a Henslow Research Fellowship. B.W. acknowledges support from the National Natural Science Foundation of China (NFSC) (grant No. 51802331), Guangdong Provincial Key Laboratory of Optical Information Materials and Technology (Grant No. 2017B030301007) and the 111 Project. T.K. acknowledges support from the Impuls- und Vernetzungsfonds der Helmholtz Gemeinschaft via the project PEROSEED. We are grateful to the UK Materials and Molecular Modelling Hub for computational resources, which is partially funded by EPSRC (EP/P020194/1). T.C.S. and D.G. acknowledge the support from the Ministry of Education AcRF Tier 2 grant MOE2016-T2-1-034 and MOE2017-T2-1-001 and from the Singapore National Research Foundation Investigatorship NRF-NRFI-2018-04. We would also like to express our sincere thanks Prof. Chao Zhang for his helpful discussions.

TOC graphical entry